Modelling the damage and deformation process in a plastic bonded explosive microstructure under tension using the Finite Element method

H. Arora[1], E. Tarleton[2], J. Li-Mayer[3], M.N. Charalambides[3*] and D. Lewis[4]

(1) The Royal British Legion Centre for Blast Injury Studies and Department of Bioengineering, Imperial College London, SW7 2AZ,
(2) Department of Materials, University of Oxford, Parks Road, OX1 3PH,
(3) Department of Mechanical Engineering, Imperial College London, SW7 2AZ,*
m.charalambides@imperial.ac.uk, Tel: +44(0)207 594 7246
(4) AWE, Aldermaston, Berkshire, RG7 4PR

Abstract

Modelling the deformation and failure processes occurring in polymer bonded explosives (PBX) and other energetic materials is of great importance for processing methods and lifetime storage purposes. Crystal debonding is undesirable since this can lead to contamination and a reduction in mechanical properties. An insensitive high explosive (PBX-1) was the focus of the study. This binary particulate composite consists of (TATB) filler particles encapsulated in a polymeric binder (KELF800). The particle/matrix interface was characterised with a bi-linear cohesive law, the filler was treated as elastic and the matrix as visco-hyperelastic. Material parameters were determined experimentally for the binder and the cohesive parameters were obtained previously from Williamson et al. (2014) and Gee et al. (2007) for the interface. Once calibrated, the material laws were implemented in a finite element model to allow the macroscopic response of the composite to be simulated. A finite element mesh was generated using a SEM image to identify the filler particles which are represented as a set of 2D polygons. Simulated microstructures were also generated with the same size distribution and volume fraction only with the idealised assumption that the particles are a set of circles in 2D and spheres in 3D. The various model results were compared and a number of other variables were examined for their influence on the global deformation behaviour such as strain rate, cohesive parameters and contrast between filler and matrix modulus. The overwhelming outcome is that the geometry of the particles plays a crucial role in determining the onset of failure and the severity of fracture in relation to whether it is a purely local or global failure. The model was validated against a set of uniaxial tensile tests on PBX-1 and it was found that it predicted the initial modulus and failure stress and strain well.

Keywords: Particulate composites, High volume fraction, Finite Element Analysis, Micromechanics, Fracture, PBX and Viscoelastic matrix composite

1. Introduction

Particle filled polymer composites can provide economic and technical advantages over other engineering materials. By reinforcing a polymeric matrix with stiffer filler particles the mechan-

ical properties of the composite can be tuned to meet specific requirements by choosing appropriate constituent phases [1].

Numerical studies on the effect of microstructure, arrangement and volume content of hard damageable inclusions in a plastic matrix on the deformation and damage growth has been conducted by Mishnaeksky [2]. He highlighted that particle arrangement does not influence the effective response of the material in the elastic region or at small plastic deformation, however it becomes significant at loads at which the particles begin to fail. The distribution of particles was shown to have significant effects based on their arrangement, with more structured arrangements having higher flow stresses compared to random or skewed/biased arrangements. The effect of increasing size caused a very strong decrease in the strain hardening rate and lead to quicker and earlier damage growth in the composites. Diler and Ipek [3] showed experimentally and numerically that increasing volume fraction and particle size of their Al-SiC_p composites reduces flexural strength, with volume fraction having a more significant effect.

Fu et al. [4] studied the effects of particle size, particle/matrix adhesion and particle loading on composite stiffness, strength and toughness of a range of particulate composites having both micro- and nano-fillers with small aspect ratios. It was shown that composite strength and toughness are strongly affected by all three factors, especially particle/matrix adhesion. This is expected, because strength depends on effective stress transfer between filler and matrix, and therefore toughness is controlled by the particle/matrix adhesion. Maloney et al. [5] reviewed previous attempts at experimentally modifying certain parameters such as filler volume fraction, stiffness and size as well as strength of both the filler and matrix to assess the effect each had on the stiffness, strength and fracture toughness of the composite. It is worth mentioning here that conventional particle reinforced composites go up to volume fractions of 50%, due to limits in what can be fabricated, which is significantly lower to that studied here.

Polymer bonded explosives (PBX) are used in a wide variety of civil and military applications such as detonators and solid rocket propellants. The volume of explosive crystals used within PBX can vary from 60% to 95% by mass [6]. The inert binder is used to reduce the shock sensitivity of the explosive and to make it safer to handle. PBX formulations can vary greatly depending on their application. Crystal/filler choices are made based upon sensitivity, energy release and achievable packing density. The matrix/binder material is used to bond these fillers together in a way such that they can achieve their potential. The binder can strongly affect the formability and fracture properties of the PBX.

The small volume of binder material can strongly influence the behaviour of the composite as there is generally a large mismatch in moduli between the stiff crystals and the binder. This binder material enables the composite to deform and absorb energy and it is this that allows the PBX to be prepared and machined to desired shapes and sizes. However it is the quality of the interface which is also a significant concern for manufacturers. Understanding the behaviour of the material on a micro-scale is essential to ensure minimal loss of the filler during processing. Finite element (FE) analysis of these microstructures allows the full-field strain map to be predicted. A knowledge of the strain field inside the filler, matrix and along the particle/matrix interface is essential to predict matrix or particle cracking and debonding between the filler and the matrix. Early works in this area include research such as that of Guild and Young [7] looking into the application of combined numerical and statistical methods to predict the elastic properties of particle filled composite materials. The model, validated against macro-scale experimentation, allowed for improved understanding of the failure process occurring on a micro-scale between glass spheres and the matrix. PBX formulations can vary greatly depending on their application and therefore require individual and unique modelling approaches.

More recently work such as that by Barua and Zhou [6] attempted to simulate large volume fraction grades of PBX. Cohesive zone finite element methods were implemented on a digitised microstructure as well as idealised geometries of particle distributions. Bimodal distributions of particle sizes produced composites with improved mechanical integrity over a monomodal distribution of particles sizes. They also highlighted that failure at the interface was more likely in regions of flat faced particles compared to round ones. Particle debonding in high filled elastomers used in solid propellants was also investigated by Matous et al [8]. They modelled particle debonding through cohesive laws and determined its effect on the macroscopic mechanical response of the composite through a small strain, multi-scale formulation. The simulations were performed using a packing algorithm, generating a unit cell matching the volume fraction and particle size distribution of the actual composites. Seidel et al [9] used a finite element code to simulate the mechanical response of LX17. Because of the highly filled nature of the material, Voronoi tessellation was used to represent the explosive crystals. The latter were surrounded by linear viscoelastic cohesive zones that represented the binder matrix. A comparison was made between their simulation results and experimental data. Yan-Qing and Feng-Lei [10] studied PBX9501 composites and employed a similar technique, i.e. the Voronoi tessellation method with a viscoelasic cohesive law at the particle interface. Cracking in the HMX particles was accounted through a tensile crack model and they validated their predictions with experimental data. Finally, purely experimental studies on PBX materials have also been reported in literature, e.g. Liu et al [11], Drodge et al [12], Chen et al [13], Thompson et al [14], Gee et al [15], Rae et al [16]. The work presented here builds on research such as this, developing a method and process for analysing actual microstructures of binary particle filled composites. In real PBX microstructures there are fine particles, which will be present in the binding material accounting for a significant portion of the filler volume fraction. This has previously been accounted for by either expanding or dilating digitised geometries [6], or through using Voronoi tesselated microstructures with viscoelastic cohesive zones. Note that in our method, the matrix and the interface are modelled separately unlike Voronoi tessellation methods. The model presented here is different to the reported literature in that it captures all large particles and models them explicitly, whilst fine particles are accounted for by increasing the stiffness of the matrix material model. This enables very high volume fraction composites to be modelled, compared to the general literature in the area focused on volume fractions below 50% for particulate filled composites. The damage criteria for fracture is also developed here and included within the analysis, allowing the complex damage development process within these particulate composites to be modelled explicitly.

2. Material constitutive laws: development and characterization

2.1. Composite materials

The PBX composition investigated here is referred to as PBX-1. This comprises a KELF800 matrix material, which is a chloro-tri-fluoro-ethylene vinylidene-fluoride co-polymer that exhibits a non-linear viscoelastic behaviour. The filler material is TATB, or triamino-trinitrobenzene, which is assumed to be a linear elastic solid. To guide the development and validate the model, the PBX was tested under uniaxial tension at 2×10^{-3}/s. Cylindrical dumbbell specimens were cast with a gauge length of 33.2 mm with a constant diameter of 10.2 mm. The densities of TATB and KELF800 are 1.94 g/cm^3 and 2.00 g/cm^3 respectively. The composite contains 95% TATB by mass fraction, equating to a 95.1% volume fraction.

Table 1 shows a summary of the tensile test results. The Young's modulus, E, failure strain, ε_f, and failure stress, σ_f, for each of the three replicate specimens are given. There is a small statistical sample collected here due to the expense, environmental considerations and hazards involved to fabricate and test these types of materials.

Table 1: Raw tensile test data for the composite material.

Sample	ε_f	σ_f (MPa)	E (GPa)
1	0.00174	8.263	7.85
2	0.00161	7.929	8.02
3	0.00189	8.567	7.11
Average	0.00174	8.253	7.66

A set of images of various magnifications were obtained prior to testing to quantify the particle size distribution visible within the finished product. These are shown in Figure 1.

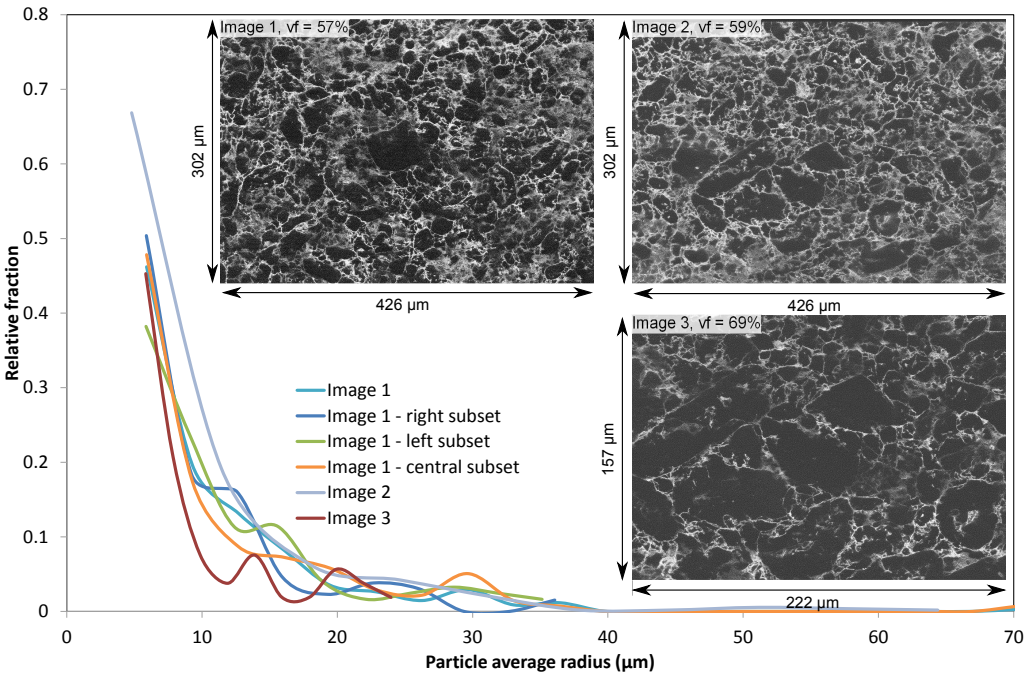

Figure 1: Three electron microscope images of PBX-1, where the dark regions (low intensity) represent the filler, TATB, and the light regions (high intensity) the matrix, KELF800. The graph shows the particle size distributions for each image as well as sub regions within Image 1.

The two phases can be identified in the sample images shown in Figure 1. Obtaining SEM images of this microstructure is a challenge compared to conventional composite materials, due to the smearing effect that is observed during sample preparation. One of the images shown in Figure 1, Image 3, was selected to generate the finite element mesh, since it was the cleanest image obtained i.e. appeared to show the highest volume fraction of crystals visible in the image, 69%, (see Figure 2). All images shown in Figure 1 were however analysed in terms of volume

fraction and particle size distribution. The volume fractions visible are comparable and ranged from 57-69%. The particle size distributions of the whole images shown in Figure 1 as well as random subsections of these images were obtained using Matlab [17] and are compared in Figure 1. These look similar and it justifies the use of the chosen image in Figure 2 as a suitable representative volume element.

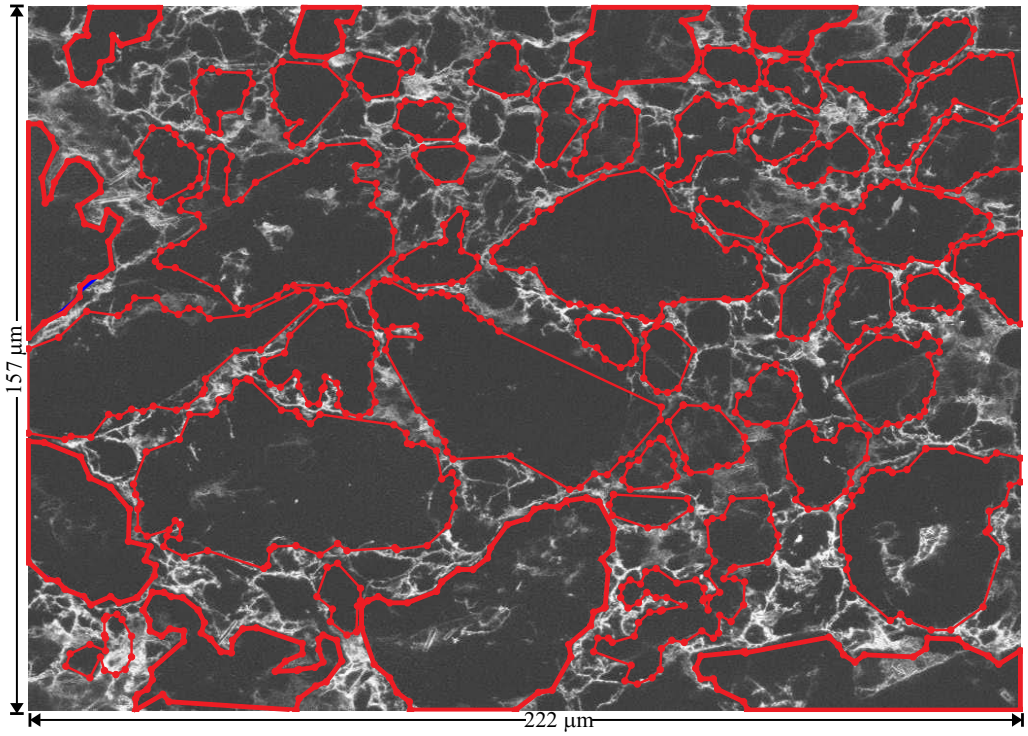

Figure 2: An electron microscope image of the PBX microstructure, where the dark regions (low intensity) represent the filler, TATB, and the light regions (high intensity) the matrix, KELF800 [18]. The set of polygons (shown in red) were used to generate the finite element mesh for the 2D polygon model.

In addition, in order to quantify the thickness of the matrix between particles, the images were analysed using Matlab [17]. A line segment was drawn in multiple locations across the image. The greyscale intensity was used to determine the boundaries of the two materials. It was found that the thickness ranged from approximately 0.83-30 μm with an average of 6 μm. The other images were not taken forward for the modelling phase since the level of detail in the edges would be lost at the lower magnifications and since the total area fraction of visible crystals was lower than that shown in Figure 2, which showed near 70% in the raw image.

2.2. *Filler material*

The filler was treated as an isotropic elastic solid with material data taken from literature [15] with a Young's modulus, $E_f = 31.5$ GPa and Poisson's ratio, $\nu_f = 0.2$. TATB has been investigated thoroughly in literature with properties widely established. Its structure is graphitic in nature and under significant shear forces these planes of preferred slip can provide significant

initiation sites for failure and fracture. However, in spite of the apparent anisotropy in TATB and given the experience with mechanical testing of this composite material and its failure behaviour, TATB is treated as a linear elastic isotropic material in this study. This is because fracture within the crystal is a secondary failure mechanism to debonding along the filler/matrix interfaces. In addition, modelling the correct anisotropy would require knowledge of the orientation of the individual crystals in the imaged microstructure. Even if such information had been available, the model complexity would increase significantly. For these reasons, we made the simplifying assumption that the filler crystals could be treated as isotopic.

2.3. Matrix material

A series of tensile tests were conducted on the KELF800 over a range of true strain rates, (10^{-4} s^{-1} $< \dot{\varepsilon} <$ 10^{-1} s^{-1}). The results are shown in Figure 3. Tensile dog-bone samples were produced in accordance to with ISO 527-2 (type 5A) standards from 2 mm thick sheets provided by the Atomic Weapons Establishment (AWE). The samples had a gauge length 30 mm and width 4 mm. These parent material sheets were produced in line with the processes used to manufacture the composite discussed in section 2.1.

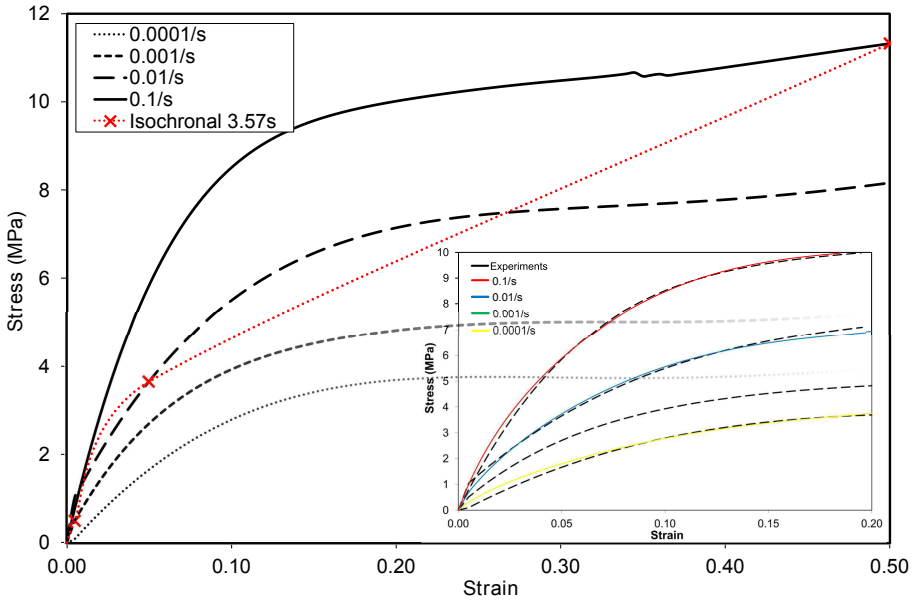

Figure 3: Plot of true stress - true strain for KELF800 binder material and the calibrated hyper-viscoelastic material model (inset).

It was assumed that all deformation occurs in the gauge length. This allowed the change in gauge length to be approximated by the machine displacement (i.e. standard travel of crosshead). The suitability of this assumption was verified optically using a line-tracking procedure. Five equally spaced lines were drawn across the gauge length of each specimen, and grey scale images were extracted from the video recordings at different points during each test. These were then analysed using the line tracker function in Matlab [17]. It was found that the strain was uniform along the gauge length for the range of relevant strains and confirmed that these were true strain rate controlled tests.

The binder material is clearly rate sensitive and exhibits a non-linear $\sigma - \varepsilon$ response, as illustrated by the example isochronal plot at a time of 3.57 s in Figure 3. However it was possible to accurately characterize the binder behaviour with a hyper viscoelastic material law which is shown in Figure 3.

Assuming a separable time- and strain-dependent material behaviour [19], [20], the relaxation stress under a step strain loading history is written as:

$$\sigma(\varepsilon, t) = \sigma_0(\varepsilon) g(t) \tag{1}$$

where $g(t)$ and $\sigma_0(\varepsilon)$ are functions of time and strain respectively. The chosen form of the time function is the Prony series [19]:

$$g(t) = c_5 + \sum_{i=1}^{4} c_i \exp^{(-t/\phi_i)} \tag{2}$$

where t and ϕ_i are time and time constants respectively, and c_i are dimensionless constants related to c_5 through $\sum_{i=1}^{4} c_i + c_5 = 1$. For an arbitrary strain history, the stress is evaluated via the Leaderman form of the superposition integral [21]:

$$\sigma(\varepsilon, t) = \int_0^t g(t-s) \frac{d\sigma_0(\varepsilon)}{ds} ds \tag{3}$$

where $\sigma_0(\varepsilon)$ is the instantaneous stress at strain ε. The van der Waals model is chosen as the hyperelastic potential [22]. The true stress form for uniaxial tension and uniaxial compression can then be described using $\sigma_0(\lambda) = \frac{\partial W}{\partial \lambda} \lambda$, where W is the hyperelastic potential and λ is the stretch ratio equal to the exponential of the current true strain ε. The stress for uniaxial tension, $\sigma_0(\varepsilon)$, can then be derived as:

$$\sigma_0(\lambda) = \mu_0^m \lambda (\lambda - \lambda^{-2}) \left[\frac{\sqrt{\lambda_m^2 - 3}}{\sqrt{\lambda_m^2 - 3} - \sqrt{\lambda^2 + 2\lambda^{-1} - 3}} - a \sqrt{\left(\frac{\lambda^2 + 2\lambda^{-1} - 3}{2} \right)} \right] \tag{4}$$

where μ_0^m is the instantaneous initial shear modulus, λ_m is the locking stretch constant and a is the global interaction parameter [23].

By substituting Eq. 2 in Eq. 3, and evaluating the integral using finite time increments [24], [25], the following form is obtained:

$$\sigma(t_{n+1}) = c_5 \sigma_0(t_{n+1}) + \sum_{i=1}^{N} \left(\exp^{-\Delta t/\phi_i} \sigma_i(t_n) + c_i \frac{1 - e^{-\Delta t/\phi_i}}{\Delta t/\phi_i} [\sigma_0(t_{n+1}) - \sigma_0(t_n)] \right) \tag{5}$$

Eq. 5 is a function for updating the stress $\sigma(t_{n+1})$ where Δt is the time increment defined as $\Delta t = t_{n+1} - t_n$ and $\sigma_i(t_n)$ is the stress corresponding to the i^{th} term of the Prony series at time t_n i.e. $\sigma_i(t_n) = \int_0^{t_n} c_i \exp(-\frac{t_n - s}{\phi_i}) \frac{d\sigma_0(s)}{ds} ds$. Eq. 5 can be used to calculate the stress at any time, t_{n+1} , provided the stress at the previous time increment, t_n, is known. The initial state at $t = 0$ is $\sigma = \varepsilon = 0$, hence the stress at $t > 0$ can be calculated. A detailed derivation is given in [19]. The function can be evaluated for various strain histories by minimizing the error between the experimental values of stress and those predicted using Eq. 5. The time constants ϕ_i are fixed. A five term Prony series was sufficient to give a good fit to experiment up to a strain of 0.2 as shown in the Figure 3 inset with instantaneous matrix shear modulus of μ_0^m=72 MPa, a locking stretch,

$\lambda_m = 2.06$ and global interaction parameter, $a = 3.96$. All parameter values are summarised in Table 2.

$\mu_0^m(MPa)$	λ	a	$\mu^*(MPa)$	
72	2.1	4.0	1200	
c_1	c_2	c_3	c_4	c_5
0.45	0.19	0.092	0.11	0.16
ϕ_1 (s)	ϕ_2 (s)	ϕ_3 (s)	ϕ_4 (s)	ϕ_5
0.1	1	10	100	∞

Table 2: Experimentally calibrated parameters for the hyper-viscoelastic binder material model.

It is not necessary or even possible to simulate every particle explicitly for high volume fractions. Analytic models have been developed [26, 27] to describe the enhancement provided by the presence of inclusions in the binder material. However care must be taken when using simplified expressions which have been derived under the simplifying assumption that the volume fraction is low and consequently do not have an explicit dependence on the elastic constants of the stiffer filler [27]. This is not the case for high volume fractions and the dependence on the filler modulus needs to be taken into account. The finite element meshes used here contained a filler volume fraction of 0.57. This is the fraction that was extracted from the microstructure image in Figure 2, when converted to a binary image. Some particles are lost at this stage, even large ones intelligible by eye due to the loss in image contrast resulting from the smearing of the polished PBX surface. Any particle under 5 μm can not be reliably identified in Figure 2. The total filler volume fraction should be 95%. Therefore the matrix must be stiffened to account for the missing volume fraction, which is assumed to be made up of very fine particles dispersed throughout the matrix. This is acceptable since debonding will occur preferentially around large particles, as the debonding stress varies as $r^{-1/2}$ [28]. Williams [29] derived an analytical model for quantifying toughening of polymers by plastic void growth. The model was based on Lamé equations for a rigid spherical particle in an elastic shell subjected to a uniform tension. Chen et al [30] also studied interfacial debonding by means of the Eshelby equivalent inclusion method. They both give results that show that for a given interface adhesion energy, the critical debonding stress varies inversely as the square root of the particle size. Further Matous et al [8] state that in their models there was a marked size effect on the failure of their particle interfaces with most of the failure occurring on large particle interfaces, even though damage initiation was size independent and that this agrees with experimental observations. Rae et al[31] studied deformation and failure of PBX composites and they also reported that failure was observed to start around the edges of larger filler particles perpendicular to the direction of tensile strain. Therefore fine particles do not debond from the matrix allowing the matrix to be treated as a homogenous composite with a volume fraction of $c^f = 0.88$; $0.57 + 0.88(1 - 0.57)$ gives the required volume fraction of 0.95. Equation (6) gives the stiffened matrix modulus which is a function of the shear modulus of both phases, the filler volume fraction (0.88) and the Eshelby transformation tensor, $S_{1212} = (4-5\nu_m)/15(1-\nu_m)$ where ν_m is the Poisson's ratio of the matrix material, 0.38, assuming a spherical shape for the inclusions [18, 32, 33, 34].

$$\mu_0^m \rightarrow \mu^* = \mu_0^m + \frac{c^f \mu_0^m}{\frac{\mu_0^m}{\mu^f - \mu_0^m} + 2(1 - c^f) S_{1212}} \tag{6}$$

Equation 6 was used to obtain μ^* (see Table 2), the fine loaded binder instantaneous shear modulus, and substituted for μ_0^m in (4). The values of the locking stretch λ_m and interaction parameter a were not modified as there is an absence of analytical models, which describe how or even if λ_m and a would vary as a function of filler volume fraction, ν_f. No fluctuations in λ_m and minimal increases in a have been shown in Latex with up to 0.25 TiO_2 filler fraction [35] but further investigations are required to investigate how larger volume fractions can influence these parameters. The assumption of spherical inclusions was explored further given the known platelet nature of the visible crystals. The effect of the aspect ratio changing from 1 to 0.25 on μ^* was seen to cause a moderate increase in μ^* from 1200 MPa in Table 2 to a maximum 1500 MPa. This was obtained using the Mori-Tanaka formulation for aligned particles and the Van Es model [36, 37] to homogenise the effect of randomised particle orientation. So even though the aspect ratio would change significantly the moduli of aligned platelets, in reality a randomised orientation of the particles would greatly lessen the effect on the effectively isotropic modulus. Given the unknown nature of the exact representative aspect ratio of the fine particles, and the fact that the variation at most could be 20%, the fine particles were assumed to be spherical and μ^* was taken to be 1200 MPa.

2.4. Interface material model

The primary failure mode which occurs within these composites is debonding along the particle-matrix interface which is only later followed by transgranular fracture of the TATB crystals and tearing of the binder. Therefore only debonding along the particle/matrix interface was considered. A bi-linear traction (σ_n) - separation ($\triangle$) cohesive law as illustrated in Figure 4 was used to simulate the interface. Literature values of the debond energy were used, namely G_c = 271 mJ/m^2, which was obtained using molecular dynamics simulations of the interface [15]. The same value is assumed for both mode I and mode II. The critical damage initiation stress σ_c was calculated based on the Atomic Force Microscope pull-off technique [38]. With knowledge of the work of adhesion and therefore the debond energy, G_c, the value of σ_c needed to debond a spherical cap of the matrix from a flat surface was measured from the pull-off force and the corresponding contact area [39]. The same value of σ_c = 13 MPa was used in both mode I and mode II i.e. $\sigma_{Ic} = \sigma_{IIc}$ = 13 MPa. The stiffness of the cohesive zone in mode I was set at, k_I =315 GPa/μm, with $k_{II} = k_I/2(1 + \nu_f)$, where ν_f is the filler Poisson's ratio, taken to be 0.2. Values of cohesive element stiffness were determined via parametric studies such that both artificial compliance and numerical convergence problems were avoided. These values comply with various guidelines proposed in the literature [40]. The thickness of the elements is not important for the global behaviour as long as it is accounted for in the stiffness calculated for the element, again to avoid undesired compliance.

The traction-separation law describes the rate at which the cohesive stiffness is degraded after damage initiation. σ_c is the criterion used here for initiation. The energy that is dissipated as a result of the damage process, i.e., the energy release rate, G_c, is equal to the area under the traction-separation curve, see Figure 4. For mixed mode loading conditions, damage is activated in the normal and shear loading modes, in terms of a maximum stress criterion expressed as:

$$\max\left\{\frac{\langle\sigma_I\rangle}{\sigma_{Ic}}, \frac{\sigma_{II}}{\sigma_{IIc}}\right\} = 1 \tag{7}$$

where the symbol $\langle\sigma_I\rangle$ represents the Macaulay bracket, defined as $\langle\sigma_I\rangle = \frac{1}{2}(|\sigma_I| + \sigma_I)$, implying that damage is not initiated in compression. As already mentioned, the energy that is

dissipated as a result of the damage process, i.e. the energy release rate, G_c, is equal to the area under the traction-separation curves, i.e. $G_{Ic} = \frac{\sigma_{Ic}\delta_{Ic}}{2}$ and $G_{IIc} = \frac{\sigma_{IIc}\delta_{IIc}}{2}$ for pure normal and shear loading conditions respectively. In addition, we assumed a linear mixed mode failure locus with the total energy release rate, G, being equal to:

$$G = G_I + G_{II}, \frac{G_I}{G_{Ic}} + \frac{G_{II}}{G_{IIc}} = 1 \tag{8}$$

where G_I and G_{II} are the energy release rates in the normal and shear directions. After the onset of damage, the elements soften until they fail, at which point they are deleted (zero stiffness). Softening causes numerical convergence issues when an implicit solver is used such as Abaqus/Standard. Simulations were therefore performed using Abaqus/Explicit. An automatic time increment with a maximum size of $\Delta t = 10^{-6}$s ensured that the kinetic energy was negligible compared to the internal energy ensuring the simulation was quasi-static. The 3D sphere model used cohesive contact for ease of mesh generation. The equivalent mesh using cohesive elements and cohesive contact were compared on a smaller scale to ensure the two methods were interchangeable without impacting the global (stress-strain) and local (failure) behaviour.

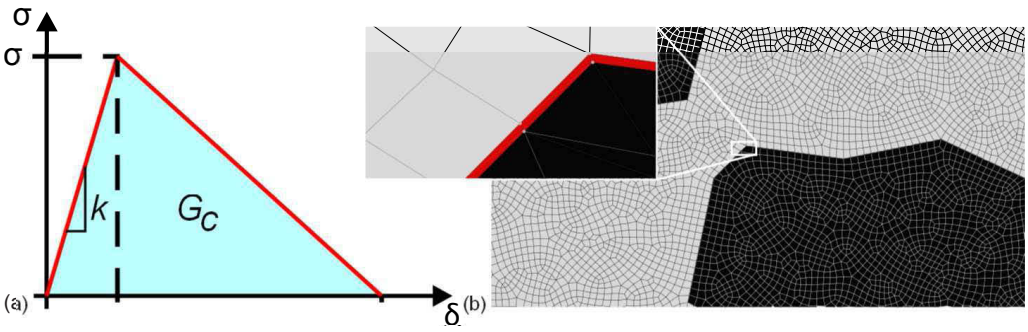

Figure 4: (a) Schematic of the bilinear traction-separation law used to define the cohesive zone behaviour of the particle/matrix interface. Part of the 2D polygon mesh shown in (b) the thin layer, 0.02μm, of cohesive elements (red) is visible in the inset.

3. Mesh generation

One of the major challenges in simulating binary composites is developing an accurate representation of the microstructure. Usually an idealised filler geometry is assumed such as circles and ellipsoids in 2D or spheres and spheroids in 3D [41],[42],[43],[44]. To investigate this assumption, an image based mesh generation algorithm was used [45] to generate a 2D mesh of the actual composite geometry by representing the TATB crystals as a set of polygons. The SEM image of the composite is shown in Figure 2 with the 53 polygons identified by the algorithm shown in red.

In addition to the 2D polygon model described above, 2D circle and 3D sphere models were included in our study. The commercial software MacroPac [46] was then used to generate a simulated microstructure with the same volume fraction (0.57) and particle size distribution as the 2D polygon mesh with the assumption that the filler is a set of 61 circles in 2D and 1164 spheres in 3D. The number of particles varies from model to model in order to maintain a similar size

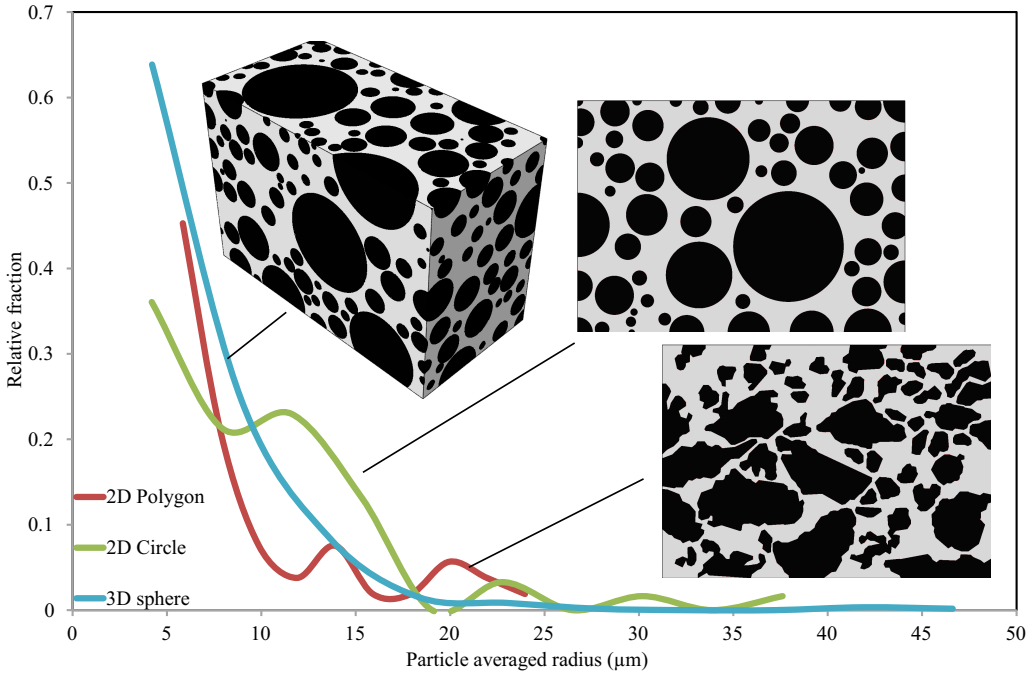

Figure 5: Particle size distributions of the TATB crystals extracted from the SEM image in Figure 2 alongside the distributions used in the 2D circle and 3D sphere models.

distribution for the given shape (see Figure 5). Due to the different packing efficiency between polygons and circles, more particles are needed in 2D circles (61) than 2D polygons (53) to attain the same overall explicitly simulated volume fraction. Similarly 1164 spheres were needed for the 3D sphere model in order to capture the particle size distribution. Note as a result of this higher number of particles, the 3D sphere particle size distribution is smoother that the 2D models as shown in Figure 5. Here it should also be acknowledged that a size distribution obtained from a 2D slice cannot be used to generate the 3D representation unless the particles are spherical [47]. In our case the particle geometry is not spherical but, in the absence of 3D imaging (difficult with micro-CT given the low density mismatch), the 2D polygon distribution was used to construct the 3D sphere model as well as the 2D circle model. The three geometries are shown in Figure 5 together with the particle size distributions.

The simulated area was $L_x \times L_y = 222 \times 157\ \mu$m in 2D and $L_x \times L_y \times L_z = 222 \times 157 \times 111\ \mu$m in 3D. A mesh convergence study was performed and a total of 692175 elements were used for the 2D circle model, and 706153 for the 2D polygon model. Linear 4 node plane stress elements with 1 integration point per element (CPS4R) were used for the matrix and filler with a thin layer (0.02μm) of 4 node cohesive elements with 2 integration points per element (COH2D4) along the interfaces. The 3D sphere mesh required a total of 29229480 linear 4 node tetrahedral elements (C3D4). The applied tensile displacement was $2 \times 10^{-3} L_y = 0.314\ \mu$m. This was applied on a ramp function such that the strain rate was the same as the experiments ($2{\times}10^{-3}$/s).

Boundary conditions can strongly affect the outcome of a given simulation, so it is important to ensure that the correct choice is made. Four different cases were investigated to simulate the

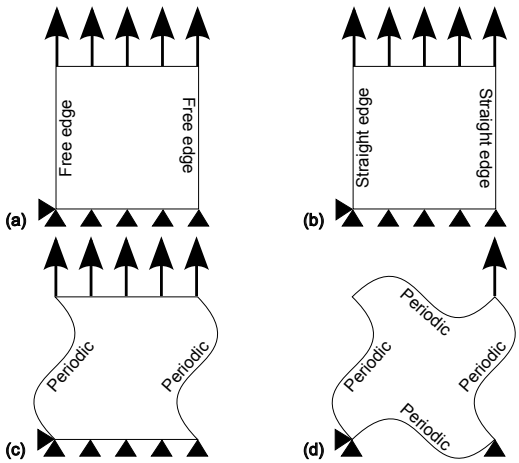

Figure 6: Schematic diagram showing the four boundary condition cases investigated.

tensile loading of the two-dimensional polygon model. The four cases were: (a) traction free vertical edges, (b) straight vertical edges $u(0, y) = u(0, L_y)$, $u(L_x, y) = u(L_x, L_y)$, (c) periodic vertical edges $u(L_x, y) = u(0, y) + u(L_x, 0)$ and (d) periodic on all 4 edges. These are illustrated schematically in Figure 6.

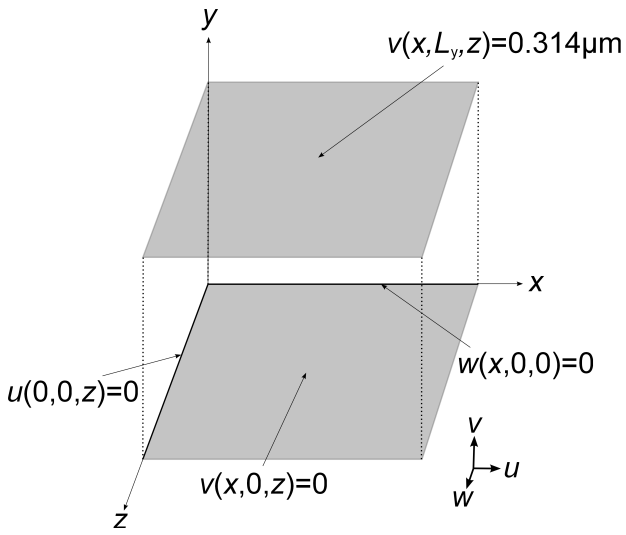

Figure 7: Schematic diagram showing the final boundary condition used for the 3D model (u, v, w are displacements in x, y and z respectively).

Results presented in [18] showed that for a sufficiently large simulated volume, the choice between cases (a), (b) and (d) of boundary conditions does not influence the macroscopic response. Case (c) showed some variation due to the mismatch of constraint applied in the two axes, leading to unnatural failures. Periodic boundary conditions are reserved for repeatable

units of material and the geometry in this study although representative of the material, is random and therefore not repeatable. Therefore all further simulations were performed using case (a) boundary conditions. In the 2D model, the node at the origin was fixed in both directions (see Figure 6). For consistency, the x and z axis were fixed in the 3D sphere models shown in Figure 7.

4. Results

The maximum principal strain field throughout the simulation is shown in Figure 7 for the 2D polygon model, the 2D circle model and a side on view of the 3D sphere model. The 2D circle and 3D sphere model results are similar at the lowest applied strain. At larger strains, the 3D model shows a higher level of damage around the large particles than the 2D model. However the largest difference between all three models is that the polygon corners in the 2D polygon model generate stress concentrations, which initiate failure along the interface and brittle fracture right through the representative element of the composite. By the end of the simulation a crack can be seen orthogonal to the loading direction in Figure 7 whereas only the largest spheres have debonded near the poles, leading to a more gradual accumulation of damage. Figure 7 shows the failure evolution for the three models. For the two models 2D polygons and 3D spheres which show macroscopic failure, debonding occurs around the larger particles. This is also observed by an earlier onset of failure and associated drop is stress in the macroscopic stress-strain response of the 2D polygon model as shown in Figure 8(a).

The experimentally measured elastic modulus and failure point are also shown in Figure 8(a). The latter are consistent with the deformation and fracture behaviour observed in the 2D polygon model which gives confidence in the validity of the latter model. From Figure 8(a), both the circle and polygon 2D models are somewhat more compliant than the 3D model as expected; this is due to the plane stress assumption in both 2D models. In order to investigate the effect of this assumption, the 2D circle and 2D polygon models were also run using plane strain elements, illustrating the two extremes that bound a 3D model behaviour in terms of the lateral deformation constraint. As shown in Figure 8(a), the plane strain conditions show a consistent lower strain to failure as compared to the plane stress results, as expected. Comparing the idealised 2D circle model and the real geometry 2D polygon model, the observed difference in the onset of failure stems from the strain concentration effects provided by the sharp corners of the polygon particles as already mentioned. Therefore the added strain localisation provided by the polygons gives a more brittle fracture behaviour and lower strain to failure, compared to the relatively progressive softening seen by the 2D circle models. The 2D polygon model therefore gives the most accurate predictions for the deformation behaviour of this particulate composite, when compared to the experimental data.

Simulations were performed at a range or strain rates as shown in Figure 9(b). The faster rate produces a stiffer response in the matrix and the critical failure stress at the interface is reached at a smaller applied macroscopic strain, whereas at lower strain rates the matrix is able to accommodate the applied strain delaying fracture at the interface. There is therefore a competition between the applied loading rate and the two mechanisms in the model by which the loading can be accommodated, either through intra-granular fracture or matrix deformation.

The crack path at the end of the simulation for the three different filler geometries is shown in Figure 10. This indicates that it is unreasonable to assume an idealised circle/sphere geometry for the filler as the filler remains bonded to the matrix near the equator preventing rapid crack propagation across the sample as observed experimentally and in the polygon model. The 2D

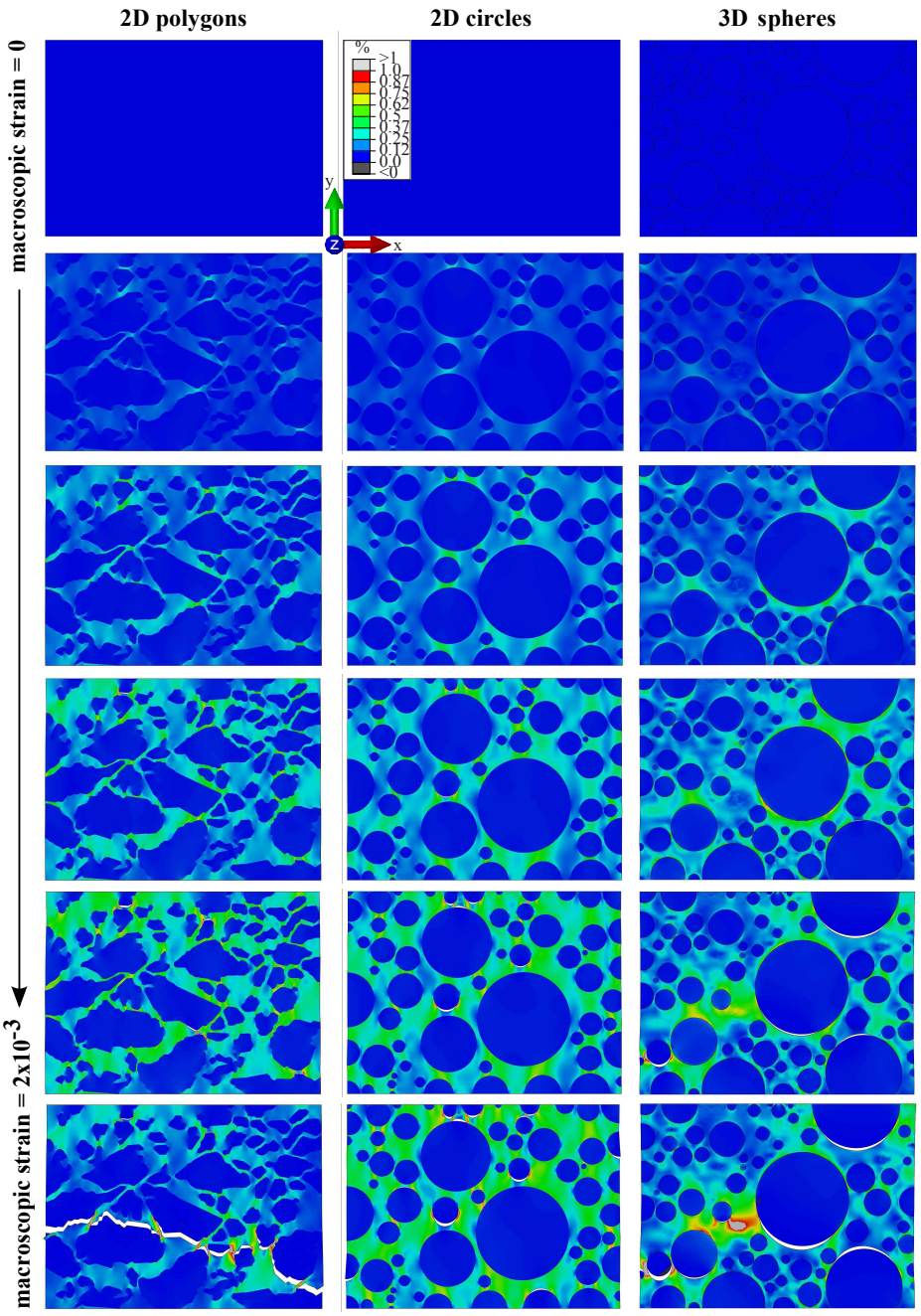

Figure 8: The maximum principal strain at equally spaced intervals of applied macroscopic strain from 0 to 2×10^{-3} (the end of the simulation) for the 2D polygons, 2D circles and 3D spheres models. The displacements scaled ×5 in the contour plots. 3D sphere images shown from the free surface (z=111μm).

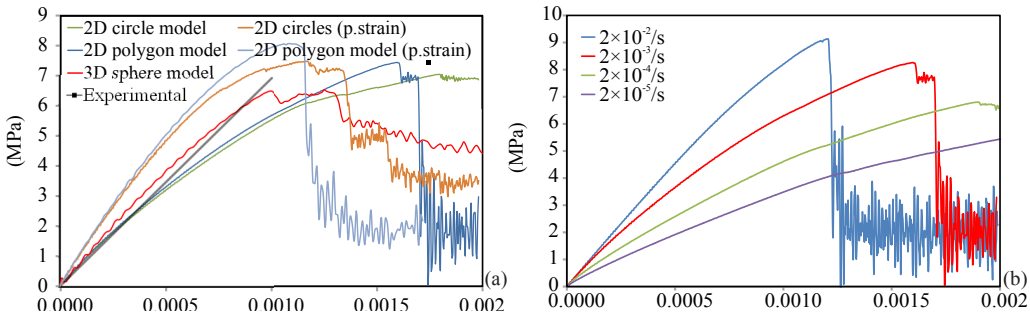

Figure 9: (a) The effect of particle geometry compared to experimental data: 2D circle, 2D polygon and 3D sphere. (b) The effect of strain rate on the behaviour of the 2D polygon model.

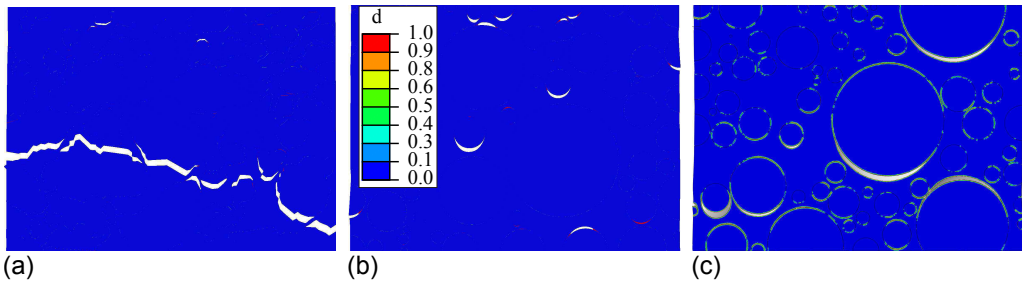

Figure 10: The scalar damage variable $0 \leq d \leq 1$ at an applied macroscopic strain of 2×10^{-3} (the end of the simulation): (a) 2D polygons, (b) 2D circles and (c) 3D spheres at free surface (z=111μm). White regions (voids) indicate the element has failed and been deleted. Displacements scaled ×20.

circle and 3D sphere models exhibited progressive softening in contrast to the 2D polygon model that exhibited brittle fracture, with a more sudden debond initiation and propagation. More energy is dissipated in the matrix in the circle and sphere models compared to the polygon model. The 3D sphere model for example in Figure 10 shows a great deal of green areas at the interfaces, meaning a more global softening is occurring compared to a localised single major debond path as seen in the 2D polygon model. Figure 11 examines the crack paths in more detail for the 3D sphere model. As expected more severe damage regions are observed in the 3D sphere model compared to the 2D circle model, given the triaxial stress state that can exist in the 3D object. However, in spite of generating apparent large debond areas, a model (3D sphere) taking into account the volume fraction, size distribution but not the shape of the particles was insufficient to capture the global $\sigma - \varepsilon$ behaviour of the composite.

To investigate the influence of model size and to ensure the model is representative, the 2D polygon model was cut into four smaller models, or RVEs (representative volume elements), the smallest being 1/16 of the original area with the same aspect ratio, material laws and equivalent boundary conditions (see Figure 12). The volume fraction of the visible particles in each of the RVE's in Figure 12 was within 4.8% of the original 2D polygon model; the total volume fraction however was kept at 95% for all RVE's through the FLB adjustment. The crack path can be seen in Figure 12 which indicates that the large particles with edges close to horizontal (where the mode I traction is greatest) fail in all cases regardless of model size. Hence the macroscopic

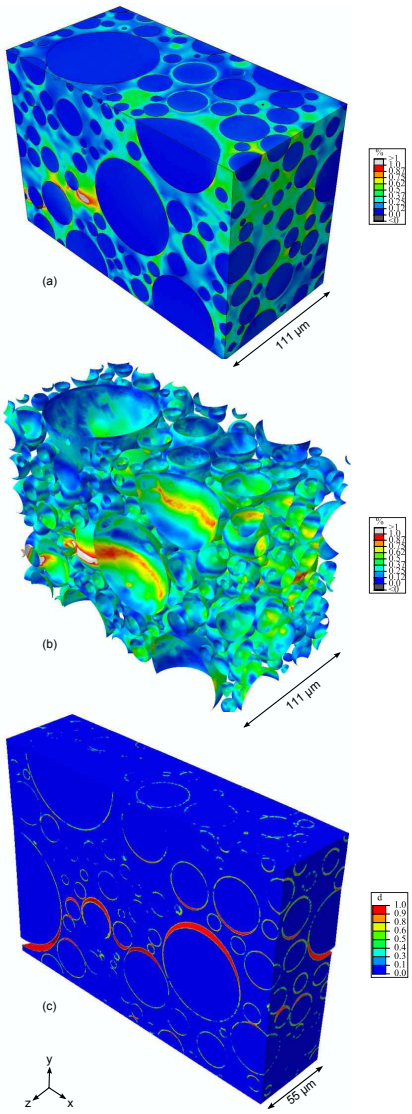

Figure 11: 3D view of the 3D sphere model at an applied macroscopic strain of 2×10^{-3} (the end of the simulation): (a) max principal strain (rotated view of Figure 8 same scale), (b) max principal strain same as (a) but plotted on the interface and (c) a section half way through along the z axis showing the scalar damage variable (similar to Figure 10(c) but at the centre instead of the free surface). Displacements scaled ×20.

response is governed by the geometry of a few filler particles. It is therefore not surprising that the macroscopic stress strain response for all model sizes were in agreement except for a small change in the elastic modulus due to slight differences in the *shapefunction*, i.e aspect ratio, number and length of edges, associated with each RVE model as shown in Figure 13(a).

For each model size, the effect of the elastic stiffness ratio of the two phases E^f/E^m, was investigated by increasing the elastic shear modulus of the matrix μ^* while keeping the filler

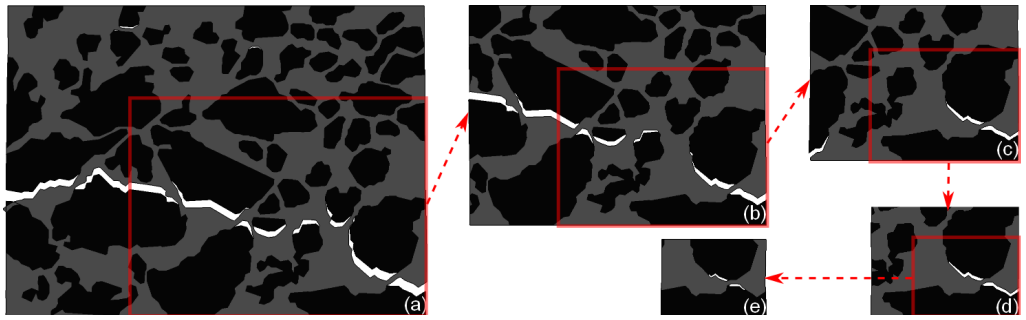

Figure 12: RVE study to examine the influence of reducing the model geometry size whilst keeping volume fraction constant. (a) Full 2D polygon model at the end of the simulation with the area reduced to (b) 1/2 (c) 1/4 (d) 1/8 (e) 1/16. Displacements ×20.

modulus constant. This is equivalent to increasing the applied strain rate which also leads to a stiffening of the matrix modulus. Consequently both the macroscopic failure stress of the composite (Figure 13(b)) and elastic modulus (Figure 13(c)) increase as the matrix stiffness approaches that of the filler.

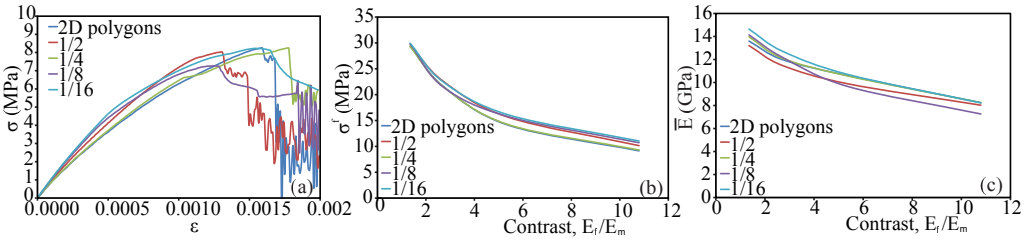

Figure 13: (a) The effect of model size on the macroscopic stress-strain response predicted with the 2D polygon model. (b) The failure stress and (c) composite modulus as a function of contrast E^f/E^m with E_f = 31.5 GPa and increasing the fine loaded initial matrix modulus, μ^*, for different model sizes.

There is an argument over whether or not the volume chosen is representative. Work by Underwood [47] debates whether a slice can be taken through any axis such that the area fraction matches the volume fraction. A step beyond that must look at whether the area of the microstructure chosen is sufficiently large to represent the global behaviour. There is a tradeoff between capturing enough particles to be representative and capturing enough detail in the particle geometry to accurately predict fracture paths and stress concentrations. It has been previously shown by Mohammed et al. [48] that for low modulus contrast, simplified representations of a geometry and a smaller RVE is suitable. This work indicates that even for a higher contrast, an RVE can consist of a small number of filler particles but that the macroscopic failure response is not accurately captured if a highly idealised filler geometry (circles or spheres) is assumed.

In terms of design considerations for general particulate composites, this study has shown that shape of the particles plays a significant role in the damage development process within the composite. If the material designer requires a brittle failure or a more gradual degradation, then this can be achieved through changing the shape of the particles. This effect of shape has been illustrated in Figure 9 and Figure 10. Design curves, such as Figure 13(b) and (c),

can be generated to inform the material designer how to tune the constituent properties of their composite to meet the demands of a specific application. For example, for a hypothetical design criterion of σ^f >15 MPa, then here E^f/E^m must be less than 4. A robust model such as this can prove a powerful tool in the design and manufacturing process.

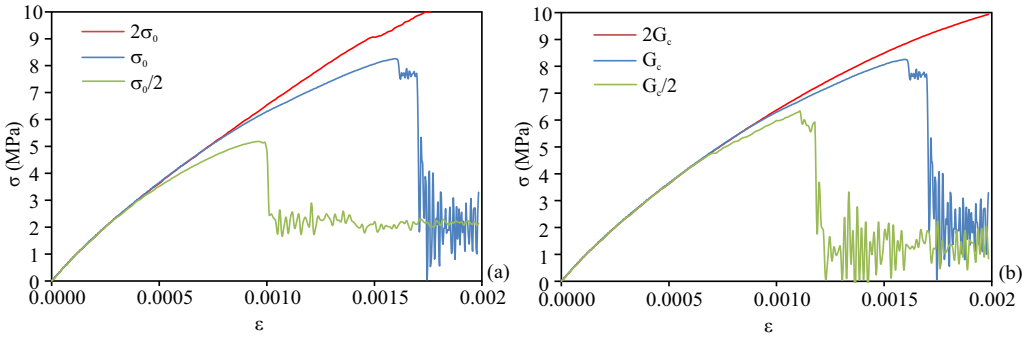

Figure 14: The effect of (a) σ_0 and (b) G_c on the 2D polygon model

Finally, the effect of the fracture energy and damage initiation stress for the cohesive zone parameters was varied to show their influence on the macroscopic failure response of the composite as shown in Figure 14. Reducing the damage initiation stress or fracture energy to half the original value means that in both cases the work of fracture is halved as the area under the stress strain curve is halved. However reducing σ_c means that damage is initiated at a lower stress as seen in Figure 14(a). When the parameters were doubled failure was not observed for the macroscopic strain applied here. This sensitivity to cohesive parameters indicates that the values used are reasonably accurate as the failure point measured experimentally agreed well with the failure predicted by the 2D polygon model (see Figure 9(a)).

5. Conclusion

A novel method for modelling the microstructure of a high volume fraction particle filled (95% TATB/KELF800) composite has been presented. An analytical micro mechanics model has been used to define the matrix behaviour which was calibrated with experimental data and stiffened to account for fine inclusions. Filler debonding was included as it is the primary failure mode expected in this material. The elastic response and failure point predicted by the model were validated against uniaxial tensile test data for the composite. The importance of an accurate representation of the filler geometry was shown. For the material laws used here, the response was independent of model size but highly sensitive to the cohesive law parameters (G_c and σ_c). Therefore detailed experiments are required to define these parameters, on the correct scale, strain range and strain rate range to reliably predict composite deformation and fracture behaviour. Even though the models were validated, the experimental data available were limited; therefore more experiments are needed in the future for the mechanical response of the PBX composite.

Acknowledgements

We thank AWE for supporting this research, our collaborators at Cambridge lead by D.M Williamson for the data provided on the cohesive parameters and the SEM images of the PBX microstructures, Prof Felicity Guild for productive discussions on finite element methods, and Mr Sandeep Palakodaty, for conducting the tensile tests on the matrix material.

References

[1] R. Rothon. *Particle-filled polymer composites*. Polymer Science and Technology Series. Longman Group Limited, 1995.

[2] L.L. Mishnaevsky Jr. Three-dimensional numerical testing of microstructures of particle reinforced composites. *Acta Materialia*, 52:4177–4188, 2004.

[3] E.A. Diler and R. Ipek. An experimental and statistical study of interaction effects of matrix particle size, reinforcement particle size and volume fraction on the flexural strength of alsi$_c$ composites by p/m using central composite design. *Materials Science and Engineering A*, 548:43–55, 2012.

[4] S-Y. Fu X-Q. Feng, B. Lauke and Y-W. Mai. Effects of particle size, particle/matrix interface adhesion and particle loading on mechanical properties of particulatepolymer composites. *Composites Part B*, 39:933–961, 2008.

[5] H.H. Kausch T. Kaiser, A.C. Maloney and H.R. Beer. Review: Parameters determining the strength and toughness of particulate filled epoxide resins. *Jounral of Material Science*, 22:381–393, 1987.

[6] A. Barua and M. Zhou. A lagrangian framework for analyzing microstructural level response of polymer-bonded explosives. *Modelling and Simulations in Materials Science and Engineering*, 19:055001, 2011.

[7] F.J. Guild and R.J. Young. A predictive model for particulate-filled composite materials: Part 1 - hard particles. *Journal of Material Science*, 24:298–306, 1989.

[8] X. Gu-D. Rypl T.L. Jackson K. Matous, H.M. Inglis and P.H. Geubelle. Multiscale modeling of solid propellants: From particle packing to failure. *Composites Science and Technology*, 67:1694,1708, 2007.

[9] K.L.E. Helms G.D. Seidel, D.H. Allen and S.E. Groves. A model for predicting the evolution of damage in viscoelastic particle-reinforced composites. *Mechanics of Materials*, 37:163–178, 2005.

[10] W. Yan-Qing and H. Feng-Lei. A micromechanical model for predicting combined damage of particles and interface debonding in pbx explosives. *Mechanics of Materials*, 41:27–47, 2009.

[11] K.X. Li-P.W. Chen Z.W. Liu, H.M. Xie and F.L. Huang. Fracture behaviour of pbx simulation subject to combined thermal and mechanical loads. *Polymer testing*, 28:627–635, 2009.

[12] S.J.P. Palmer-W.G. Proud D.R. Drodge, D.M. Williamson and R.K. Govier. The mechanical response of a pbx and binder: combining results across the strain-rate and frequency domains. *J. Phys. D: Appl. Phys.*, 43:335403, 2010.

[13] F. Huang P. Chen and Y. Ding. Microstructure, deformation and failure of polymer bonded explosives. *J Mater Sci*, 42:5272–5280, 2007.

[14] R. Deluca D.G. Thompson and G.W. Brown. Time-temperature analysis, tension and compression in pbxs. *Journal of Energetic Materials*, 30:299–323, 2012.

[15] R.H. Gee A. Maiti, S. Bastea and L.E. Fried. Molecular dynamics investigation of adhesion between tatb surfaces and amorphous fluoropolymers. *Macromolecules*, 40:3422–3428, 2007.

[16] H.T. Goldrein-J.E. Field P.J. Rae, S.J.P. Palmer and A.L. Lewis. Quasi-static studies of the deformation and failure of pbx 9501. *Proc. R. Soc. Lond. A.*, 458:2227–2242, 2009.

[17] MathWorks. *MATLAB - Documentation*. www.mathworks.com/help/techdoc/, matlab 7.12.0 (r2011a) edition, 2011.

[18] H. Arora-E. Tarleton M.N. Charalambides, D.M Williamson and C.L. Leppard. An image based approach to modelling plastic bonded explosives (pbx) on the micro scale. Montreal, Canada, July 2013. Proceedings of International Conference on Composite Materials, ICCM19.

[19] S.M. Goh M.N. Charalambides and J.G. Williams. Determination of the constitutive constants of non-linear viscoelastic materials. *Mechanics of Time-Dependent Materials*, 8:255–268, 2004.

[20] M.N. Charalambides-S.M. Goh L. Wanigasooriya, J.G. Williams and S. Chakrabarti. Large deformation extensional rheology of bread dough. *Rheol. Acta*, 46:239–248, 2006.

[21] J.G. Williams. *Stress Analysis of Polymers*. John Wiley, London, 1980.

[22] H. G. Kilian and T. H. Vilgis. Fundamental aspect of rubber elasticity in real networks. *Colloid and Polym. Sci.*, 262:15–21, 1984.

[23] Simulia. *Abaqus 6.9*. www.simulia.com, version 6.9 edition, 2009.

[24] R.L. Taylor K.S. Pister and G.L. Goudreau. Thermomechanical analysis of viscoelastic solids. *Int. J. Numer. Met. Eng.*, 2:45–59, 1970.

[25] M. Kaliske and H. Rothert. Formulation and implementation of three dimensional viscoelasticity at small and finite strains. *Comput. Mech.*, 19:228–239, 1997.

[26] E.W.S. Hagan-M.N. Charalambides C.R.T. Young, T.J.S. Learner and S. Hackney. Tensile properties of latex paint films with tio2 pigment. *Mechanics of Time-Dependent Materials*, 13(2):149–161, 2009.

[27] E.W.S. Hagan-M.N. Charalambides C.R.T. Young, T.J.S. Learner and S. Hackney. Influence of the inorganic phase concentration and geometry on the viscoelastic properties of latex coatings through the glass-transition. *Polymer*, 52:1662–1673, 2011.

[28] O.A. Stapountzi M.N. Charalambides and J.G. Williams. Micromechanical models for stiffness prediction of alumina trihydrate (ath) reinforced poly (methyl methacrylate) (pmma): Effect of filler volume fraction and temperature. *Composites Science and Technology*, 69:2015–2023, 2009.

[29] J.G. Williams. Particle toughening of polymers by plastic void growth. *Composites Science and Technology*, 70:885–891, 2010.

[30] Z-Z. Yu Z. Huang J-K. Chen, G-T. Wang and Y-W. Mai. Critical particle size for interfacial debonding in polymer/nanoparticle composites. *Composites Science and Technology*, 70:861–872, 2010.

[31] S.J.P. Palmer J.E. Field P.J. Rae, H.T. Goldrein and A.L. Lewis. Quasi-static studies of the deformation and failure of β-hmx based polymer bonded explosives. *Proc. R. Soc. Lond. A.*, 458:743–762, 2002.

[32] C.P. Tandon and G.J. Weng. The effect of aspect ratio of inclusions on the elastic properties or unidirectionally aligned composites. *Polymer Composites*, 5:327–333, 1984.

[33] B.E. Clements and E.M. Mas. Dynamic mechanical behavior of filled polymers. i. theoretical developments. *Journal of Applied Physics*, 90:5522–5534, 2001.

[34] E.M. Mas and B.E. Clements. Dynamic mechanical behavior of filled polymers. ii. applications. *Journal of Applied Physics*, 90:5535–5541, 2001.

[35] E.W.S. Hagan. *The Viscoelastic Properties of Latex Artist Paints*. Phd, Imperial College of Science, Technology and Medicine, 2009.

[36] J. Van Turnhout E. Van der Giessen S. Al-Malaika M. Van Es, F. Xiqiao and A.W. Golovoy. *Specialty polymer additives: principles and applications*. MA Blackwell Science, 2001.

[37] O.A. Stapountzi. *Stiffness and Fracture Properties of Alumina Trihydrate Filled Poly (Methyl Methacrylate) Composites*. Phd, Imperial College of Science, Technology and Medicine, 2010.

[38] S.J.P. Palmer A.P. Jardine D.M. Williamson, N.R. Hamilton and C. Leppard. Thermodynamic work of adhesion measurements of polymer bonded explosive constituents via the wilhelmy plate technique and their application to afm pull-off experiments. *Journal of Physics: Conference Series*, 500:112068, 2014.

[39] K.L. Johnson. *Contact Mechanics*. Cambridge University Press, Cambridge, 1985.

[40] A.T. Travesa. *Simulation of delamination in composites under quasi-static and fatigueloading using cohesive zone models*. Phd, Universitat de Girona, 2006.

[41] D. Sodhani and S. Reese. Finite element-based micromechanical modeling of microstructure morphology in filler-reinforced elastomer. *Macromolecules*, 47:3161–3169, 2014.

[42] D.J. Bray P. Dittanet K. Masania R.A. Pearson F.J. Guild, A.J. Kinloch and A.C. Taylor. The modelling of the toughening of epoxy polymers via silica nanoparticles: The effects of volume fraction and particle size. *Polymer*, 54:7022–7032, 2013.

[43] V. Kukshal S. Gangwar and A. Patnaik. Experimental and finite element analysis of mechanical and fracture behavior of sic particulate filled a356 alloy composites: Part i. *Proc IMechE Part L: J Materials: Design and Applications*, 0:1–15, 2014.

[44] Y. Chen H. Chen X. Peng Z. Guo X, Shi and P. Harrison. Mechanical modeling of incompressible particle-reinforced neo-hookean composites based on numerical homogenization. *Mechanics of Materials*, 70:1–17, 2013.

[45] E. Tarleton, M.N. Charalambides, and C. Leppard. Image-based modelling of binary composites. *Computational Materials Science*, 64:183–186, 2012.

[46] Intelligensys. *MacroPac*. www.intelligensys.co.uk/macropac, 7.1 edition, 2012.

[47] E.E. Underwood. *Quantitative Stereology*. Addison-Wesley Publishing Company, Reading, Massachusetts, 1970.

[48] M.A.P. Mohammed E. Tarleton, M.N. Charalambides and J.G. Williams. Mechanical characterization and micromechanical modeling of bread dough. *Journal of Rheology*, 57(1):249–272, 2013.

LaTeX Source Files

Click here to download LaTeX Source Files: elsarticle.cls